



## ORIGINAL ARTICLE

# High performance pliable supercapacitor fabricated using activated carbon nanospheres intercalated into boron nitride nanoplates by pulsed laser ablation technique

M. Hassan<sup>a,b</sup>, M.A. Gondal<sup>a,b,\*</sup>, E. Cevik<sup>c</sup>, T.F. Qahtan<sup>a</sup>, A. Bozkurt<sup>d</sup>,  
M.A. Dastageer<sup>a</sup>

<sup>a</sup> Laser Research Group, Physics Department & Center of Excellence in Nanotechnology, King Fahd University of Petroleum & Minerals (KFUPM), Mail Box 5047, Dhahran 31261, Saudi Arabia

<sup>b</sup> K.A.CARE Energy Research and Innovation Center, King Fahd University of Petroleum & Minerals, Dhahran 31261, Saudi Arabia

<sup>c</sup> Department of Genetics Research, IRMC, Imam Abdulrahman Bin Faisal University, PO Box:1982, Dammam 31441, Saudi Arabia

<sup>d</sup> Department of Physics, IRMC, Imam Abdulrahman Bin Faisal University, 1982, PO Box:1982, Dammam 31441, Saudi Arabia

Received 24 April 2020; accepted 18 June 2020

Available online 25 June 2020

## KEYWORDS

Activated carbon;  
Boron nitride;  
Nanocomposite;  
Pulsed laser ablation;  
Supercapacitor;  
Energy storage

**Abstract** Pliable supercapacitor, yielding specific capacitance ( $C_s$ ) and energy density as high as  $348 \text{ F g}^{-1}$  and  $48.3 \text{ Wh Kg}^{-1}$  respectively was fabricated using modified activated carbon electrodes. The nanospheres of activated carbon (AC) were anchored on the nanoplates of boron nitride (BN) by employing the facile technique of pulsed laser ablation in liquid (PLAL) using 532 nm focused laser beam. Four different variants of electrode materials were synthesized by varying the weight percentage (1%, 3%, 5% and 10%) of BN in AC in the PLAL precursor solution. The morphological characteristics, the elemental composition and the structural analysis of the synthesized electrode materials were studied respectively by FESEM, XPS and XRD. The morphological studies indicated that the PLAL synthesis of the electrode materials resulted in proper intercalation of carbon nanospheres into BN nanoplates, which resulted in the observed enhanced performance of the fabricated supercapacitor. Four supercapacitors in this work were fabricated using the four variants of synthesized electrode materials in conjunction with gel polymer electrolyte (GPE). GPE are well known for their non-corrosive nature and best sealing ability to avoid any leakage that results in increasing the cycle life of the device. The performance of the fabricated

\* Corresponding author at: Laser Research Group, Physics Department & Center of Excellence in Nanotechnology, King Fahd University of Petroleum & Minerals (KFUPM), Mail Box 5047, Dhahran 31261, Saudi Arabia.

E-mail address: [magondal@kfupm.edu.sa](mailto:magondal@kfupm.edu.sa) (M.A. Gondal).

Peer review under responsibility of King Saud University.



Production and hosting by Elsevier

supercapacitors was evaluated using cyclic voltammetry (CV), galvanostatic charge discharge (GCD) measurement and electrochemical impedance spectroscopy (EIS). The results indicate that the supercapacitor fabricated using 3% BN in AC as electrode material manifested the best specific capacitance and energy density. Also it was found that the supercapacitor maintained 85% of its initial capacitance even after 5000 charge/discharge cycles.

© 2020 The Authors. Published by Elsevier B.V. on behalf of King Saud University. This is an open access article under the CC BY-NC-ND license (<http://creativecommons.org/licenses/by-nc-nd/4.0/>).

## 1. Introduction

The development in modern electronics including smart, portable and wearable electronic devices strongly depends on the efficiency of the energy storage units. Ultracapacitors (also known as supercapacitors), are fascinating energy storage devices with several positive traits including high power density, better cycling ability, fast charging and safe use (Liu et al., 2019; Xiao et al., 2020; Y. Zhang et al., 2019b). Supercapacitors fabricated using porous active carbon and its derivatives are called electrochemical double layer capacitor (EDLC), storing charges electrostatically between active material and electrolyte interface (Jing et al., 2020b; Wu and Zhu, 2017). Another type of supercapacitor that uses metal oxides and conducting polymers as active material is called pseudocapacitor where the charges are stored by reversible redox reaction (Choi et al., 2019; Huang et al., 2018; Xing et al., 2018a). There is another type of supercapacitors called battery supercapacitor hybrid. They composed of capacitive electrode and battery type electrode involving Faradaic reaction on one electrode and non-Faradaic reaction on the other electrode (Xing et al., 2018b). They gain high power density from capacitive electrode and high energy density from the battery type electrode (Pham et al., 2019; Yu et al., 2020; Zhao et al., 2018).

Carbon based supercapacitors are well-known because of their high surface area, good conductivity, chemical stability and low cost (Zhai et al., 2019). The specific capacitance of a supercapacitor depends mainly on the shape, size and porosity of the electrode active material. These parameters can be controlled through careful composition of different materials or by choosing a suitable synthesis technique (W. Li et al., 2016a; Zheng et al., 2018, 2020). Many composites of carbon with metal oxides and conductive polymers have been prepared and applied as active material in the fabrication of high capacitance and high energy density supercapacitors (Abioye et al., 2017; He et al., 2019; Liu et al., 2020; Wang et al., 2020; Xu et al., 2017). It has been observed that when carbon is composited with different heteroatoms including boron (Li et al., 2019), nitrogen (Jin et al., 2015; Y. Wu et al., 2020b), sulfur (Wu et al., 2002), nitrogen sulfide (Ma et al., 2014), and nitrogen phosphide (Nasini et al., 2014), exhibits promising electrochemical properties. These improvements are attributed to the presence of additional functional groups that change the surface properties of the carbon electrodes (Jing et al., 2020a; Lu et al., 2017). It allows the ions from the electrolyte to utilize the maximum available surface area with better pore accessibility.

Recently, boron nitride (BN) has gained a lot of attention in electrochemical applications because of its graphene-like structure having atomically smooth surface, chemical and thermal stability and excellent dielectric properties (Xue et al.,

2013). The insulating characteristics of BN make it unfavorable for most of the electronic applications, if used alone. But the careful composition of BN with different conductive materials significantly changes its electrical properties (Ci et al., 2010). Li et al (Lu et al., 2017) have reported a  $C_s$  value of  $108\text{F g}^{-1}$  at  $0.5\text{ A g}^{-1}$  of AC based supercapacitor using KOH as an electrolyte. The  $C_s$  value reached to  $176\text{F g}^{-1}$ , when AC is co-doped by BN. A composite between hexagonal BN and graphene has proven to be suitable for atomically thin circuitry as explained by Levendorf et al (Levendorf et al., 2012). Nayak et al (Maity et al., 2019) have recently reported BN based ternary nanocomposites namely BN/GO/PANI, BN/rGO/PANI and BN/CNT/PANI for electrochemical energy storage applications. The highest  $C_s$  value of  $387.5\text{F g}^{-1}$  was achieved for BN/CNT/PANI ternary composite at  $1\text{ A g}^{-1}$ . But the use of CNT and PANI may restrict the commercialization of the device because of the high cost and complex synthesis method.

On the other hand, pulsed laser ablation in liquid (PLAL) has emerged as an effective and versatile technique to synthesize nanoparticles of unlimited variety with various compositions (oxides, nitrides, hydroxides, alloys etc.) and morphologies (nanospheres, nanorods, quantum dots etc.) (Zeng et al., 2012). PLAL generated nanoparticles are used in various research fields including catalysis (Blakemore et al., 2013), photocatalysis (Gondal et al., 2016; Moqbel et al., 2018a), solar cells (Ilyas et al., 2016), linear and nonlinear optics (Papagiannouli et al., 2015; Zeng et al., 2010), energy storage (Xie et al., 2016) and biomedical applications (Baati et al., 2016; Fazio et al., 2016). One of the major advantages of applying PLAL process is that the size and shape of the particles can be controlled by varying different parameters such as beam energy, laser intensity, pulse duration and by introducing external fields (Moqbel et al., 2018b).

In this work, we report the synthesis of BN/AC nanocomposite using facile and clean method of pulsed laser ablation in liquid (PLAL). The supercapacitor device was prepared using the as-synthesized BN/AC nanodispersion as electrode active material and poly (2-acrylamido-2-methyl-1-propanesulfonic acid) or simply PAMPS as gel polymer electrolyte. All the fabricated supercapacitors were characterized electrochemically through CV, GCD and EIS. The highest  $C_s$  value of  $348\text{F g}^{-1}$  was achieved for BN3 (3% BN in AC) supercapacitor, at a current density of  $0.3\text{ A g}^{-1}$  using GCD analysis.

## 2. Experimental

### 2.1. Chemicals and materials

The materials and reagents used in this experiment were of analytical grade. They include Boron nitride (BN), Nitric acid

(HNO<sub>3</sub>) and sulfuric acid (H<sub>2</sub>SO<sub>4</sub>), purchased from Sigma–Aldrich whereas, Polyvinylidene fluoride (PVDF), N-Methyl-2-pyrrolidone (NMP), Timical super C65 conductive carbon (CC) and activated carbon (AC) were purchased from MTI Corp. Deionized water was used as a solvent for the synthesis of nanocomposites.

### 2.2. Synthesis of nanocomposites using PLAL

PLAL method was used to prepare four different composites of BN with AC in increasing concentration of BN as (1%, 3%, 5% and 10% by weight in AC) and labeled as BN1, BN3, BN5 and BN10 respectively. First, AC and 10 wt% of CC were dispersed in NMP solvent through sonication, followed by the addition of BN in pre-defined concentrations. The mixture was sonicated for further 1 h to make homogeneous dispersion. The homogenized dispersion was irradiated by a laser beam of 532 nm wavelength (second harmonic of Nd-YAG laser -Brilliant B), 350 mJ pulse energy, 5 ns pulse duration with 10 Hz repetition rate for 30 min as shown by a schematic diagram in Fig. 1a. During the irradiation process, the precursor mixture was vigorously stirred using a magnetic stirrer to preserve homogeneity in the ablated sample.

### 2.3. Supercapacitor electrode fabrication

BN/AC nanodispersion obtained from PLAL process was further mixed with PVDF binder followed by stirring for 1 h using magnetic stirrer. This step is important to prepare a thick

texture that could be coated on a metallic electrode. Finally, the as-prepared paste was coated onto an aluminum current collector using an automatic coater (MRX Shenzhen) and left to dry for several hours in a vacuum oven at 80 °C. The final mass loading of the active material coated on the substrate was measured to be 0.57 mg/cm<sup>2</sup>.

### 2.4. Nano material characterization

The structural and crystallographic properties of the prepared composites were examined by X-ray diffraction technique (XRD) using Bruker advance-D8 diffractometer with Cu K<sub>α</sub> rays with wavelength ( $\lambda = 0.15416$  nm). The morphology of the samples including shape and size of the nanoparticles were investigated using high-resolution scanning electron microscope (FE-SEM) and FEI-Morgani-268 transmission electron microscope (TEM). X-ray photoelectron spectroscopy (XPS) was used to study the elemental composition and chemical environments of the laser irradiated samples using ESCALAB-250Xi machine with Al K<sub>α</sub> radiation. The aluminum sheets coated with as-synthesized nanocomposites were used in XPS analysis.

### 2.5. Fabrication and electrochemical measurements of supercapacitors

The supercapacitor device was assembled in Al/AC-BN/ GPE / AC-BN/Al configuration, where PAMPS was used as a gel polymer electrolyte (GPE). BN/AC electrodes were cut into

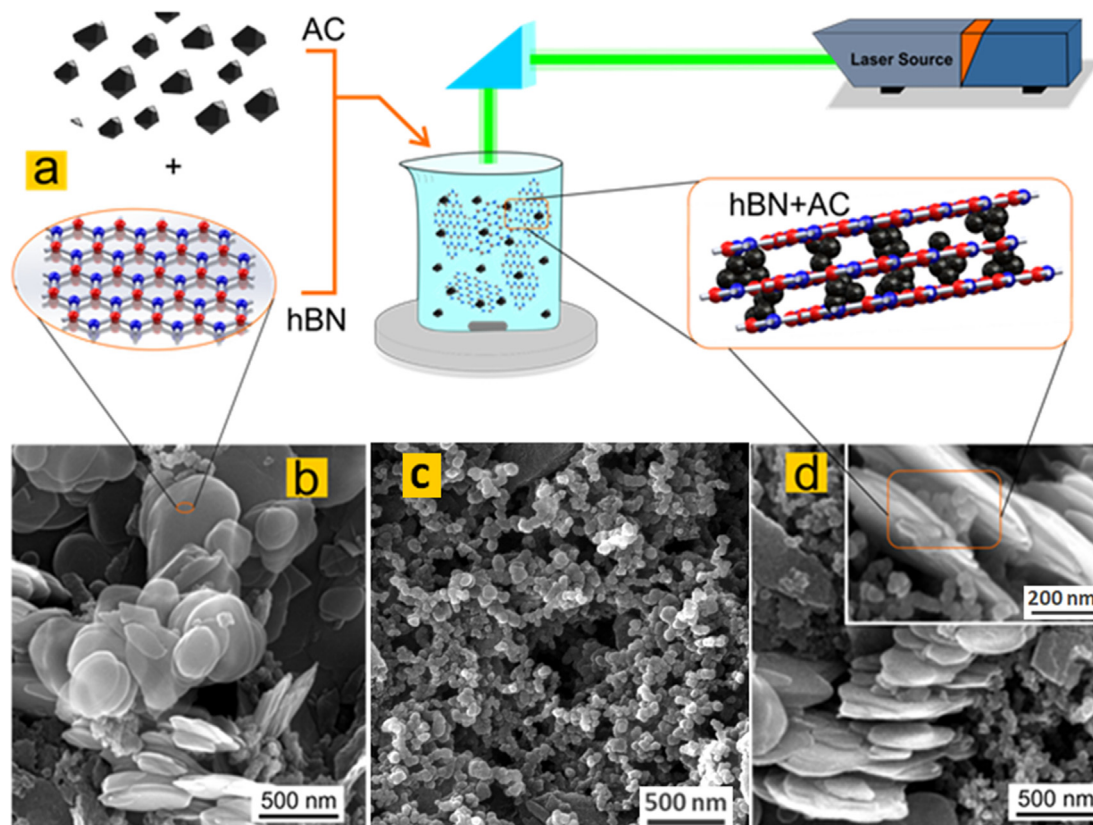


**Fig. 1** (a) Schematic of the nano synthesis using PLAL setup, High-resolution SEM images of (b) pure hexagonal BN nanoplates, (c) pure AC nanospheres, (d) BN3 demonstrating intercalated structure between AC and BN.

circular disks using Hi-throughput pneumatic disk cutter (MSK-180SC) and placed in Swagelok cell kit to perform electrochemical characterization. CV and EIS analysis for the fabricated supercapacitors were performed using potentiostat (PGSTAT302N, Metrohm Autolab). The CV of the supercapacitor cells was performed at various scan rates ranging from  $10 \text{ mV s}^{-1}$  to  $200 \text{ mV s}^{-1}$ . On the other hand, GCD analysis was performed by charging and discharging the device in the range of 0 V to 1 V using Battery analyzer (MTI corp.) at different values of discharging current. The specific capacitances ( $C_s$ ) of the fabricated supercapacitors were calculated by determining the discharging time ( $\Delta t$ ) for the supercapacitor to go through the voltage decline of ( $\Delta V$ ), at a particular discharging current ( $I$ ) according to Eq. (1) (Cevik et al., 2019; Peng et al., 2019);

$$C_s = 2 \times \frac{I \times \Delta t}{m \times \Delta V} \quad (1)$$

As we are measuring the specific capacitance of the electrode,  $m$  represents the mass of the active material coated on either of the electrode. Equation (2) and (3) are used to calculate the energy density ( $E_d$ ) and power density ( $P_d$ ) of the fabricated supercapacitors respectively (Peng et al., 2019; X. Zhang et al., 2019a).

$$E_d = \frac{1/2 \times C_s \times \Delta V^2}{3.6} \quad (2)$$

$$P_d = \frac{E \times 3600}{\Delta t} \quad (3)$$

### 3. Results and discussion

#### 3.1. Material characterizations

The morphological characterization of the laser ablated samples was performed using FESEM at different magnifications and corresponding high-resolution images are presented in Fig. 1(b, c, d). Fig. 1b shows the laser ablated sample of pure BN with structure similar to nanoplates whereas, Fig. 1c shows the nanospheres of pure AC obtained after 30 min of continuous laser ablation. The large concentration of BN shows a larger amount of these nanoplates that form a stacked structure with no spaces among them. A similar phenomena (i.e. stacking) is often observed in the synthesis of graphene sheets that lead to decrease its effective surface area. There are a few reports about preventing such aggregation by anchoring different nano particles between the sheets (Z. Wu et al., 2010b; Yan et al., 2010).

Similarly, a unique intercalated structure is obtained by dispersing BN and AC in NMP solvent and ablating the sample for 30 min using laser pulses as presented in Fig. 1d. PLAL method is capable of producing nanostructures in unique configuration with remarkable properties as reported by many researchers for different applications (Barcikowski and Compagnini, 2013; Shih et al., 2017; Walter et al., 2010). The main reason for such versatility in nanomaterial synthesis using PLAL configuration, is the formation of liquid confined plasma with high atomic densities. Such plasma, generated under high temperature and high pressure conditions, gives

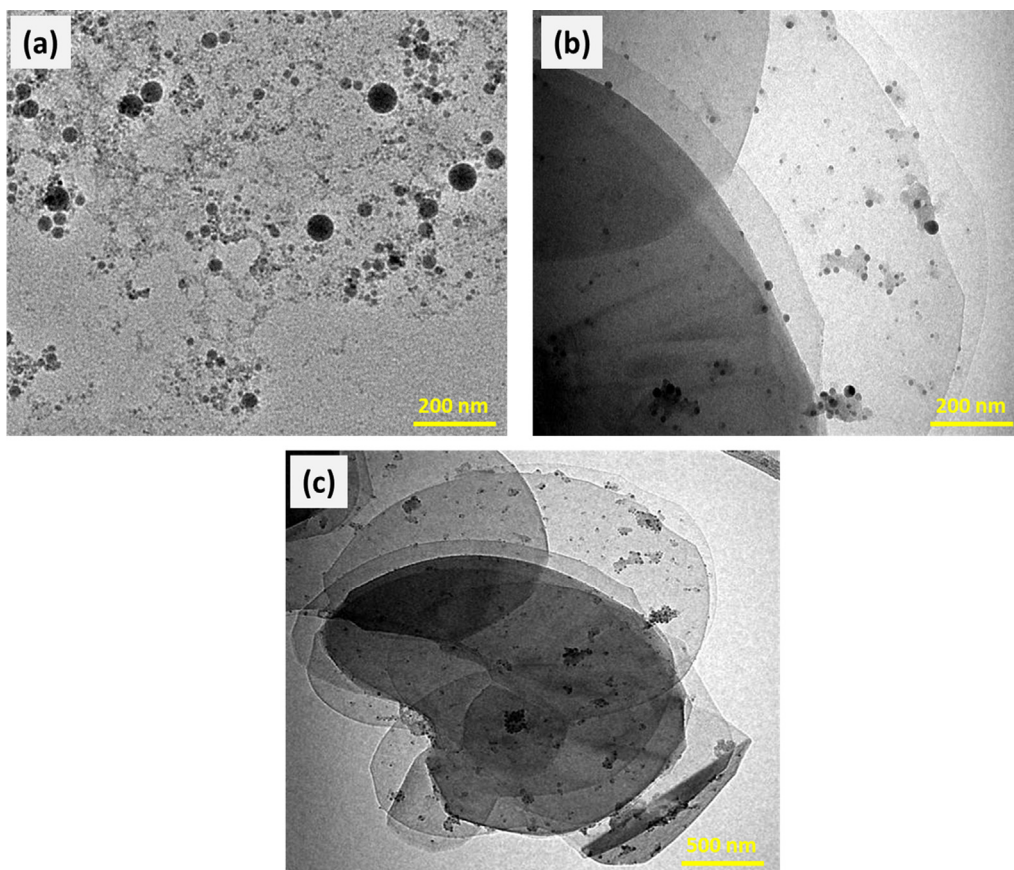
rise to the formation of new material phases with distinct properties.

Fig. 2 shows TEM images of AC and BN/AC intercalated structure formed after laser ablation process. AC nanospheres of various sizes ranging from 10 nm to 80 nm are shown in Fig. 2a. Fig. 2 (b, c) demonstrates the TEM images at different magnifications for BN/AC nanocomposite formed after laser ablation process. The composited structure is in good agreement with the proposed intercalated structure between BN and AC. The nanospheres of AC are well dispersed among the layers of BN nanoplates preventing them from stacking. The difference in the color of nanospheres is attributed to the different height levels because of the presence of BN layers.

Crystallographic study for pure BN, Pure AC, BN5 and BN10 samples was performed using powder XRD technique with 2-theta angle ranging from  $10^\circ$  to  $80^\circ$  and presented in Fig. 3a. The major peaks obtained in case of BN at an angle of  $2\theta = 26.7, 41.6, 55.0$  and  $76.1^\circ$  were indexed as (002), (100), (004) and (110) planes respectively, representing hexagonal structure of the BN corresponding to (Card No: 45-0893) (Saha et al., 2015). XRD pattern for AC shows a broad peak in the range of  $23^\circ$  to  $26^\circ$  that is minimized by the high intensity aluminum (Al) peaks. Al peaks were detected with high counts because of the porous structure of AC coated on it. XRD pattern for BN5 and BN10 samples present the major peak of AC along with a distinct (002) peak of BN.

A noticeable shift in (002) peak of BN has been observed in BN5 and BN10 sample that is presented in Fig. 3b in a narrow range of 2-theta angle. This shift in BN peak in BN/AC composite samples is attributed to the change in the lattice parameters of the BN crystal. The d-spacing was calculated to be 0.333 nm for (002) peak of pure BN crystal using Bragg's formula, that is in good agreement with the card data and published work (Kang et al., 2013). The corresponding lattice parameter "c" was calculated to be 0.667 nm for hexagonal BN crystal. The new values of d-spacing and lattice parameter were estimated to be 0.329 nm and 0.658 nm respectively for BN/AC composite structure corresponding to same (002) peak of hexagonal BN. The change in the lattice parameter "c" and d-spacing is attributed to the distortion in the lattice structure caused by the foreign elemental invasion (C.-C. Wu et al., 2010a; Yang et al., 2016). This indicates the development of new hierarchical intercalated structure of AC nanospheres with BN nanoplates.

XPS analysis of the laser ablated sample (BN/AC nanocomposite) was performed to study the chemical composition and presented in Fig. 4. Fig. 4a shows a wide survey scan for the sample BN3 with peaks labeled by the corresponding elemental symbols. The deconvoluted elemental peaks for each element in the nano dispersion including boron (B), nitrogen (N), carbon (C), oxygen (O) and fluorine (F) have been shown separately in Fig. 4b, c, d, e and f. Prior to elemental analysis, a small area from the sample surface was etched for 30 s in order to remove any contaminations participating from the air molecules. It is observed that pure boron elemental 1 s peak (188 eV) has been shifted towards higher binding energy along with splitting into two sub-peaks with binding energy 189.9 eV and 190.9 eV corresponding to B-C and B-N respectively as shown in Fig. 4b (Lu et al., 2017). The presence of major peak at 190.9 eV suggests that B and N are bonded mainly as B-N



**Fig. 2** TEM images of (a) AC nanospheres, (b, c) intercalated structure between BN nanoplates and AC nanospheres at different magnifications.

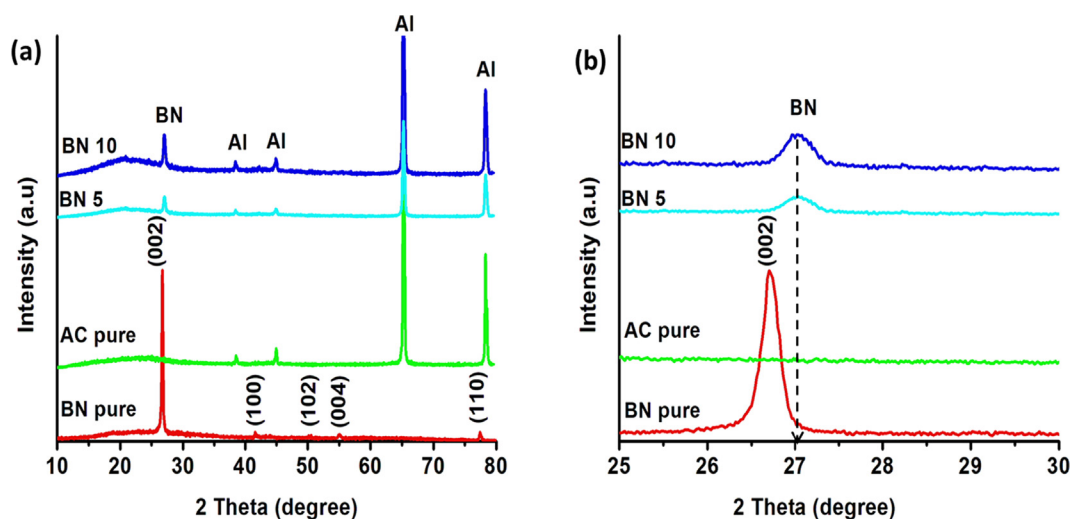


**Fig. 3** (a) XRD analysis for AC, BN, BN5 and BN10 samples, (b) Magnified image to show the peak shift of BN/AC samples.

and less intense peak at 189.9 eV corresponds to the partial formation of B-C with  $sp^2$  hybridization in the synthesized sample of BN3 (Panchakarla et al., 2007). Fig. 4c shows the elemental spectrum for N 1 s that is deconvoluted into three peaks corresponding to 397.4 eV, 398.1 eV and 400.1 eV respectively for BN, CN and NH (Liu et al., 2016). The minor

peak of N-H bonding suggests the presence of small amount of PVDF in the mixture that is participating in making bonds with nitrogen and carbon. Fig. 4d represents C 1 s spectrum that is deconvoluted into three major peaks and two minor peaks at binding energy of 284.1 eV, 284.4 eV, 285.2 eV, 287.0 and 290.3 eV respectively. The intense peaks at

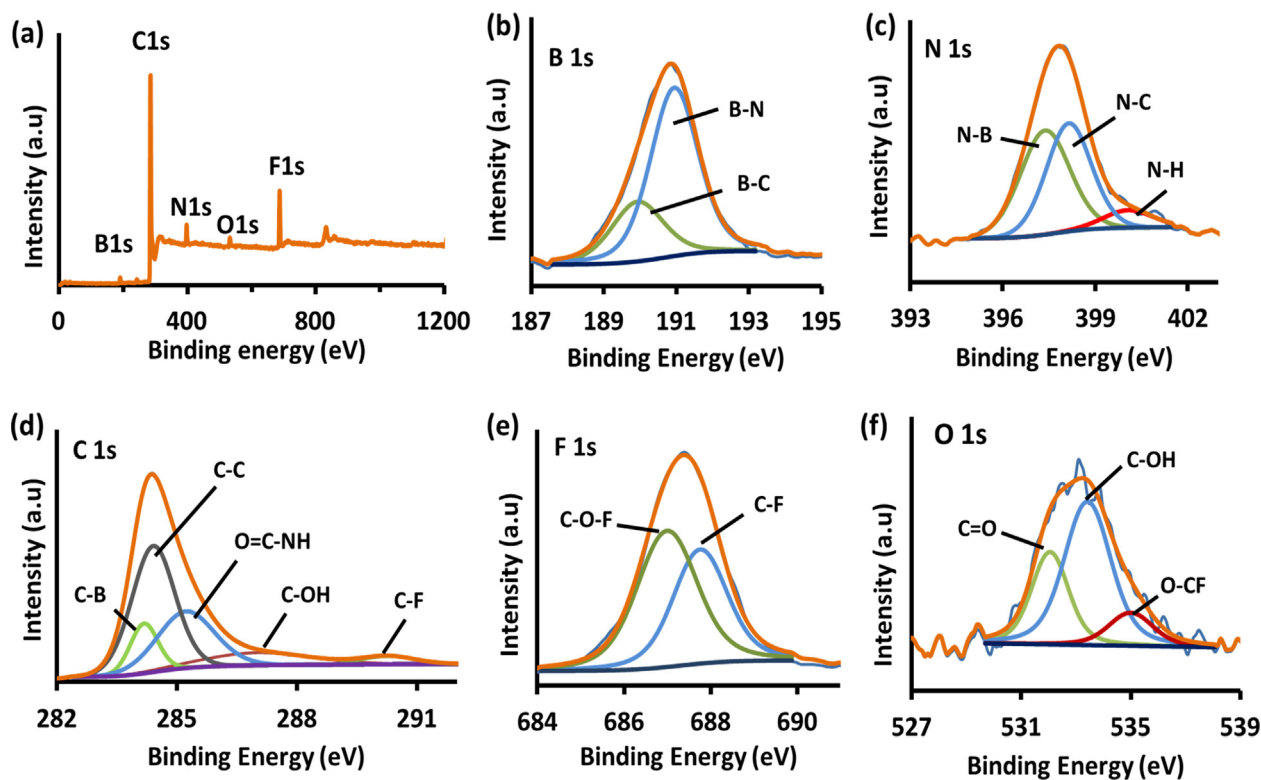


**Fig. 4** XPS spectra analysis of BN3 electrode with (a) wide scan, (b) B element, (c) N element, (d) C element, (e) F element and (f) O element.

284.1 eV, 284.4 eV and 285.2 eV are attributed to C-B, C-C and O = C-NH bonds respectively (Yang et al., 2015). The less intense peak at 287.0 eV could be attributed to C-OH bonds and 290.3 eV peak to the formation of C-F bond contributing from PVDF binder. Elemental analysis for F 1 s is shown in Fig. 4e, where F peak is deconvoluted into two sub peaks at 686.9 eV and 687.8 eV corresponding to C-O-F and C-F bonds respectively (Yun et al., 2007). The O 1 s elemental spectrum is fitted with three peaks at binding energies of 532.1 eV, 533.4 eV and 535.0 eV corresponding to C = O, C-OH and C-O-F respectively (Bartnik et al., 2012) as shown in Fig. 4f. Most of the O peaks are originated because of the presence of O in the solvent NMP ( $C_5H_9NO$ ) used. A minor contribution from the atmospheric oxygen is also detected that may be deposited on the sample surface as moisture.

### 3.2. Electrochemical characterizations

Electrochemical performance of all the fabricated supercapacitor devices was studied through CV, GCD and EIS using PAMPS electrolyte. PAMPS is a polymeric electrolyte that makes gel like texture through cross linkage, when dissolved in water. Although it is poorly soluble in most of the organic solvents including dichloromethane and acetonitrile, but the presence of sulfonic acid group makes it soluble in water to exhibit gel structure (Sonmez et al., 2005). It shows good stability in aqueous medium with superior proton conductivity (Cevik et al., 2019). Fig. 5 shows the CV of the BN/AC supercapacitors at  $40 \text{ mV s}^{-1}$  scan rate in a potential range of 1 V. The CV curves for low concentration of BN in AC electrode indicate a rectangular pattern that corresponds to the ideal

supercapacitive behavior as shown in Fig. 5a. BN3 supercapacitor exhibits the highest specific current of  $0.9 \text{ A g}^{-1}$  as compare to other supercapacitors at  $40 \text{ mV s}^{-1}$  scan rate. The adsorption and desorption of ions on the surface of the electrodes for BN3 supercapacitor obtained through CV analysis at increasing scan rates are presented in Fig. 5b. The CV scans showed an ideal capacitive behavior with excellent cyclic reversibility at all the scan rates. The maximum specific current drawn through the supercapacitor reached  $1.8 \text{ A g}^{-1}$  at  $200 \text{ mV s}^{-1}$  scan rate in 1 V potential window.

EIS was performed to study the frequency response of the fabricated supercapacitor by drawing Nyquist plot, as shown in Fig. 5c, 5d. The high frequency region of the plot shows a semi-circle whose x-intercept gives equivalent series resistance (ESR), which corresponds to the interface resistance between the electrode active material and the current collector (X. Wu et al., 2020a). The ESR value is measured to be 3.4, 2.7, 2.8 and 3.3 Ohm for BN1, BN3, BN5 and BN10 supercapacitors respectively as shown in Fig. 5d. The radius of the semi-circle approximates the charge transfer resistance ( $R_{ct}$ ) of the device (Jing et al., 2020c). These values were measured to be 1.3, 0.6, 0.7 and 2.7 Ohm for BN1, BN3, BN5 and BN10 supercapacitors respectively. The low frequency region of the Nyquist plot (Fig. 5c) shows a linear trend with slope close to  $45^\circ$  demonstrating ideal capacitive behavior arising from the electric double layer effect because of higher concentration of AC. The small deviation from the ideal capacitive behavior at low frequency is attributed to the presence of BN functional group in the AC skeleton. Moreover, the curve at low frequency indicates the Warburg resistance (W), which is the measure

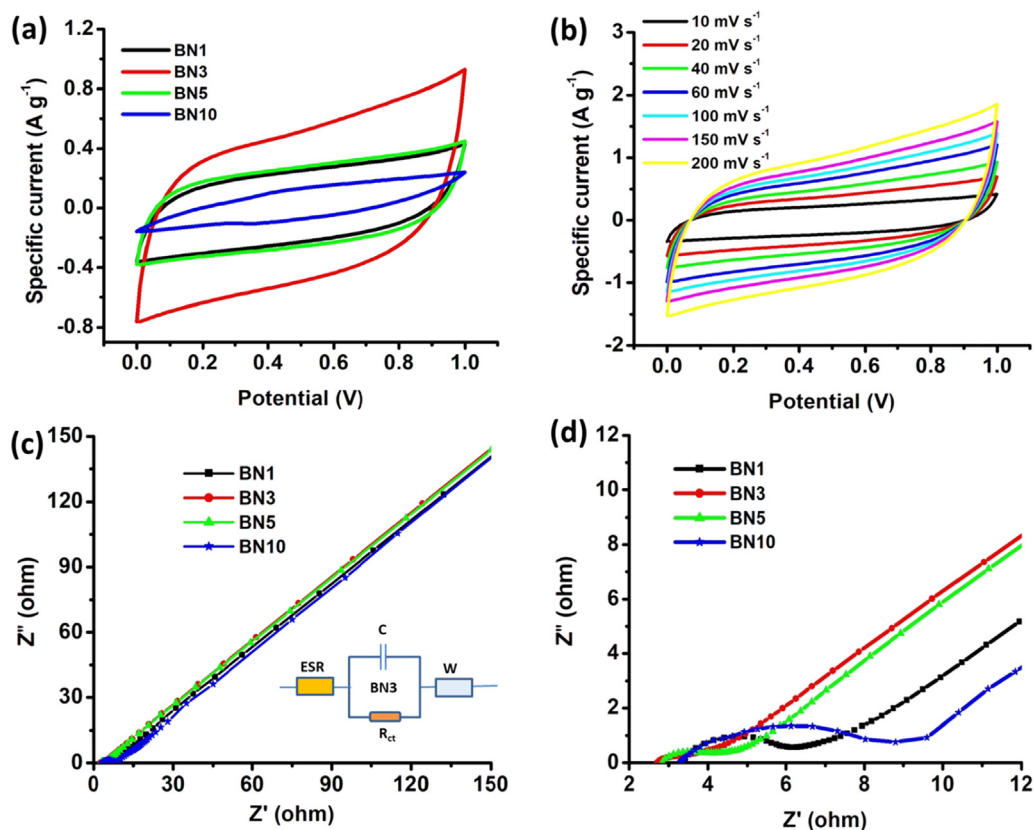


**Fig. 5** (a) Cyclic voltammetry comparison between different wt% of BN in AC, (b) CV of BN3 at different scan rates, (c) Nyquist plot, (d) Nyquist plot in high frequency range.

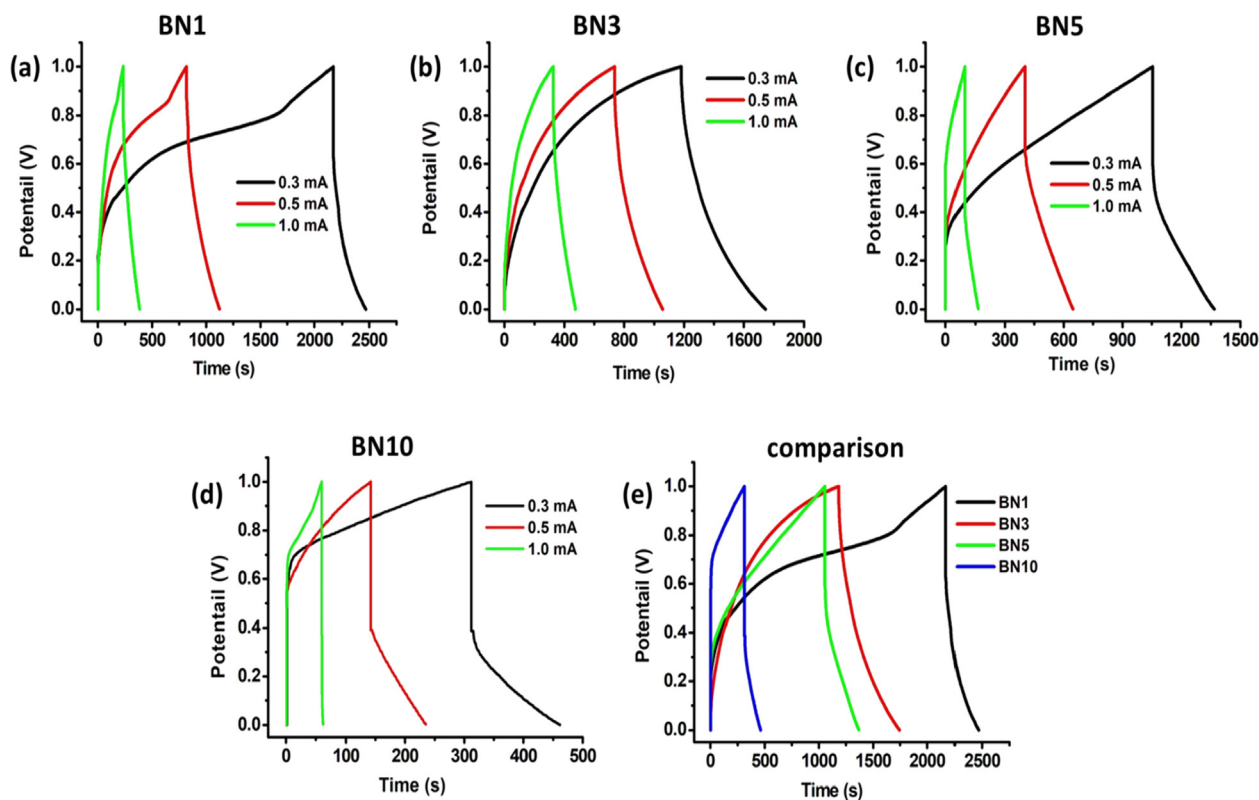


**Fig. 6** GCD analysis for (a) 1%BN, (b) 3%BN, (c) 5%BN and (d) 10%BN in AC electrode supercapacitors. (e) A comparison between all fabricated supercapacitors at a constant current density of 0.3 A g<sup>-1</sup>.

of ion diffusion ability into the pores of the electrode surface (Cheng et al., 2020). The inset of Fig. 5c shows the equivalent circuit model of BN3 supercapacitor obtained

by fitting the EIS Nyquist plot. It is clear from the Nyquist plot that BN3 electrode demonstrates the lowest ESR and lowest  $R_{ct}$  values comparing to other samples of BN in AC.

**Table 1** A comparison between all the fabricated supercapacitor electrodes at  $0.3 \text{ A g}^{-1}$  (or  $0.3 \text{ mA}$ ) of constant current density.

Fabricated supercapacitor electrodes	Areal capacitance ( $\text{mF cm}^{-2}$ )	Specific capacitance ( $\text{F g}^{-1}$ )	Energy density ( $\text{Wh Kg}^{-1}$ )	Power density ( $\text{W Kg}^{-1}$ )
BN1	103.7	183.6	25.6	292
BN3	196.6	348.0	48.3	298
BN5	106.7	189.0	26.1	301
BN10	95.9	169.8	23.6	265

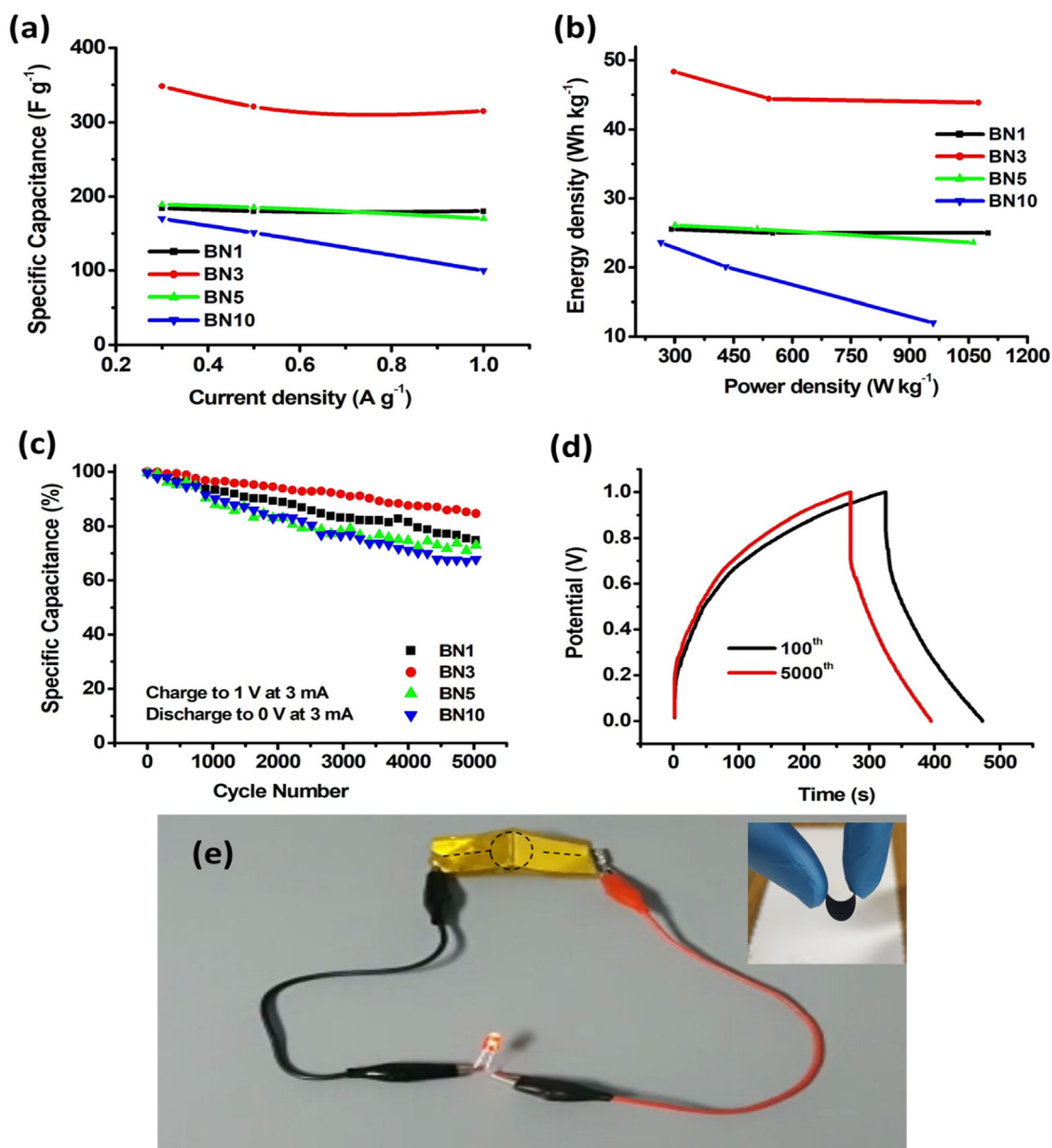


**Fig. 7** (a)  $C_s$  as a function of discharging current density, (b) Ragone plot for all the fabricated supercapacitors, (c) Capacitance retention at  $0.3 \text{ mA}$  for 5000 cycles (d) Charging and discharging curves after 100<sup>th</sup> and 5000<sup>th</sup> cycles, and (e) Photograph of LED powered by a single BN3 supercapacitor in bending state with an inset photograph showing flexibility.

**Table 2** Specific capacitance, energy density and power density of the reported supercapacitors using activated carbon and its nanocomposites.

S.N	Electrode materials	Electrolyte	Specific capacitance (F g <sup>-1</sup> )	Energy density (Wh Kg <sup>-1</sup> )	Power density (W Kg <sup>-1</sup> )	Ref.
1	BN	KCl	33.8	–	–	(Maity et al., 2019)
2	AC	PVA/PVP/H <sub>2</sub> SO <sub>4</sub>	218	4.9	–	(Yadav et al., 2020)
3	BN doped AC	KOH	176	9.7	2000	(Lu et al., 2017)
4	BN/RGO	KOH	140	–	–	(Gao et al., 2015)
5	h-BN/C	KOH	250	17	245	(Li et al., 2019)
6	BN/G (1:2)	KOH	134	2.1	1998.5	(Zheng et al., 2019)
7	Porous Carbon/ N & S	KOH	298	21	180	(Y. Li et al., 2016b)
8	Carbon hollow spheres/ N & P	KOH	232	7.84	600.5	(Lv et al., 2018)
9	3%BN/AC	PAMPS	348	43.9	1075	Present work

GCD analysis was performed for the fabricated supercapacitors at various current densities of 0.3, 0.5 and 1 A g<sup>-1</sup> as presented in Fig. 6a–d. The supercapacitor was charged from 0 V to 1 V and then allowed to discharge to 0 V at a constant current density. The  $C_s$  values for the fabricated supercapacitors were calculated from the discharging time, discharging current and the potential window using eq. (2). The  $C_s$  values for BN1, BN3, BN5 and BN10 are calculated to be 184, 348, 189 and 170F g<sup>-1</sup> respectively. It is noticeable that the highest value of  $C_s$  is achieved for BN3 supercapacitor that is in good agreement with the cyclic voltammogram, where BN3 supercapacitor shows the highest current density in the potential window of 1 V. The BN1 supercapacitor electrode took sufficiently long time to charge itself to 1 V but the discharging time was quite short. Similarly when the concentration of BN was increased to 3%, the supercapacitor took short charging time and long discharging time as compare to BN1 supercapacitor shown in Fig. 6b. As we further increase the concentration of BN, the charging time of the supercapacitor is decreased rapidly while giving rise to an IR drop in the device as given in Fig. 6c and 6d. IR drop is an important factor controlling the overall efficiency of a supercapacitor. It introduces an asymmetric behavior in charging and discharging profile that leads to energy dissipation during cycling (Pell and Conway, 2001). The presence of an IR drop at a higher concentration of BN is attributed to the stacked structure with low surface area and insulating nature of BN specie. The fact is evident from a recent reported where the  $C_s$  value of a pure BN supercapacitor was measured to be 33.75F g<sup>-1</sup> that is much lower than its other composite parts (Maity et al., 2019). For further comparison, the calculated values of  $C_s$ ,  $E_d$  and  $P_d$  at 0.3 A g<sup>-1</sup> are given in table 1.

The specific capacitance ( $C_s$ ), energy density ( $E_d$ ) and power density ( $P_d$ ) values of the fabricated supercapacitors were calculated using eq. (1), (2) and (3) respectively. The  $C_s$  value of BN1, BN3, BN5 and BN10 supercapacitors were calculated at different current densities including 0.3, 0.5 and 1 A g<sup>-1</sup> and plotted as a function of current density as shown in Fig. 7a. It was observed that BN3 supercapacitor shows the highest  $C_s$  value at 0.3 A g<sup>-1</sup> that decreases slightly with an increase in the current density and obtains stability at higher current densities. BN1 and BN5 supercapacitors show a stable behavior at all current densities with negligible change in the  $C_s$  values. However, BN10 exhibits a gradual decrease in the  $C_s$  values with an increase in current density that is attributed to the higher concentration of insulating BN. Fig. 7b shows Ragone plot of the fabricated supercapacitors at different cur-

rent densities. The highest  $E_d$  value of 48.3 Wh kg<sup>-1</sup> was exhibited by BN3 supercapacitor at a  $P_d$  value of 298 W kg<sup>-1</sup>. Whereas, the maximum  $P_d$  value of 1075 W kg<sup>-1</sup> was achieved for the same supercapacitor at 1 A g<sup>-1</sup>. The important parameters of some of the reported carbon/hetro-atomic supercapacitors are summarized in table 2.

The stability of the fabricated supercapacitors was studied for 5000 cycles of charging and discharging at 3 mA current. The specific capacitances of the supercapacitors were calculated at various cycles then converted to percentage retention and plotted as a function of cycle number as shown in Fig. 7c. BN3 supercapacitor has demonstrated excellent stability by retaining more than 80% of its initial capacitance value after 5000 cycles. This result is in good agreement with the CV and EIS analysis already explained in this work. Moreover, the GCD curve of BN3 supercapacitor for the initial 100th cycle and the final 5000th cycle is shown in Fig. 7d. These two curves show a very small difference of capacitance between them even after 5000 uninterrupted cycles of charging and discharging. From these results, it can be concluded that BN3 supercapacitor exhibits excellent stability as compare to its other composite partners. Hence 3% concentration of BN in AC can be regarded as an optimized concentration for symmetric supercapacitor configuration. Furthermore, a successful attempt has been made to light a red LED using a single BN3 supercapacitor under bending conditions as shown in Fig. 7e. The LED remained lighted for several seconds.

#### 4. Conclusion

A rapid, single step and environmental friendly method of pulsed laser ablation in liquid was employed to obtain a unique intercalation between nanospheres of AC and nanoplates of BN. A substantial enhancement in the specific capacitance of the fabricated supercapacitor was observed, in case of BN3 (3% of BN in AC) supercapacitor that is attributed to the formation of intercalated structure between AC and BN nanocomposite. The fabricated flexible supercapacitor yields  $C_s$  value as high as 348F g<sup>-1</sup> and capable of retaining 85% of the initial capacitance even after 5000 charge discharge cycles. A low power red LED was also lighted using a single BN3 supercapacitor.

#### Declaration of Competing Interest

The authors declared that there is no conflict of interest.

## Acknowledgement

The authors acknowledge the funding support provided by the King Abdullah City for Atomic and Renewable Energy, Saudi Arabia, through project KACARE 182-GSGP-06 and KACARE 182-RFP-02. The authors are also thankful to King Fahd University of Petroleum & Minerals, Saudi Arabia for funding support through project # RG 181002.

## References

- Abioye, A.M., Noorden, Z.A., Ani, F.N., 2017. Synthesis and characterizations of electroless oil palm shell based-activated carbon/nickel oxide nanocomposite electrodes for supercapacitor applications. *Electrochim. Acta* 225, 493–502.
- Baati, T., Al-Kattan, A., Esteve, M.-A., Njim, L., Ryabchikov, Y., Chaspoul, F., Hammami, M., Sentis, M., Kabashin, A.V., Braguer, D., 2016. Ultrapure laser-synthesized Si-based nanomaterials for biomedical applications: in vivo assessment of safety and biodistribution. *Sci. Rep.* 6, 1–13.
- Barcikowski, S., Compagnini, G., 2013. Advanced nanoparticle generation and excitation by lasers in liquids. *Phys. Chem. Chem. Phys.* 15, 3022–3026.
- Bartnik, A., Lisowski, W., Sobczak, J., Wachulak, P., Budner, B., Korczyk, B., Fiedorowicz, H., 2012. Simultaneous treatment of polymer surface by EUV radiation and ionized nitrogen. *Appl. Phys. A* 109 (1), 39–43. <https://doi.org/10.1007/s00339-012-7243-5>.
- Blakemore, J.D., Gray, H.B., Winkler, J.R., Müller, A.M., 2013. Co<sub>3</sub>O<sub>4</sub> nanoparticle water-oxidation catalysts made by pulsed-laser ablation in liquids. *ACS Catal.* 3, 2497–2500.
- Cevik, E., Bozkurt, A., Hassan, M., Gondal, M.A., Qahtan, T.F., 2019. Redox-Mediated Poly (2-acrylamido-2-methyl-1-propanesulfonic acid)/Ammonium Molybdate Hydrogels for Highly Effective Flexible Supercapacitors. *ChemElectroChem* 6, 2876–2882.
- Cheng, Y., Zhang, Y., Jiang, H., Dong, X., Meng, C., Kou, Z., 2020. Coupled cobalt silicate nanobelt-on-nanobelt hierarchy structure with reduced graphene oxide for enhanced supercapacitive performance. *J. Power Sources* 448, 227407.
- Choi, C., Ashby, D.S., Butts, D.M., DeBlock, R.H., Wei, Q., Lau, J., Dunn, B., 2019. Achieving high energy density and high power density with pseudocapacitive materials. *Nat. Rev. Mater.*, 1–15.
- Ci, L., Song, L., Jin, C., Jariwala, D., Wu, D., Li, Y., Srivastava, A., Wang, Z.F., Storr, K., Balicas, L., 2010. Atomic layers of hybridized boron nitride and graphene domains. *Nat. Mater.* 9, 430.
- Fazio, E., Santoro, M., Lentini, G., Franco, D., Guglielmino, S.P.P., Neri, F., 2016. Iron oxide nanoparticles prepared by laser ablation: Synthesis, structural properties and antimicrobial activity. *Colloids Surfaces A Physicochem. Eng. Asp.* 490, 98–103.
- Gao, T., Gong, L.J., Wang, Z., Yang, Z.K., Pan, W., He, L., Zhang, J., Ou, E.C., Xiong, Y., Xu, W., 2015. Boron nitride/reduced graphene oxide nanocomposites as supercapacitors electrodes. *Mater. Lett.* 159, 54–57. <https://doi.org/10.1016/j.matlet.2015.06.072>.
- Gondal, M.A., Suliman, M.A., Dastageer, M.A., Chuah, G.-K., Basheer, C., Yang, D., Suwaiyan, A., 2016. Visible light photocatalytic degradation of herbicide (Atrazine) using surface plasmon resonance induced in mesoporous Ag-WO<sub>3</sub>/SBA-15 composite. *J. Mol. Catal. A Chem.* 425, 208–216.
- He, H., Xia, Q., Wang, B., Wang, L., Hu, Q., Zhou, A., 2019. Two-dimensional vanadium carbide (V<sub>2</sub>CT<sub>x</sub>) MXene as supercapacitor electrode in seawater electrolyte. *Chinese Chem. Lett.*
- Huang, F., Meng, R., Sui, Y., Wei, F., Qi, J., Meng, Q., He, Y., 2018. One-step hydrothermal synthesis of a CoS<sub>2</sub>@ MoS<sub>2</sub> nanocomposite for high-performance supercapacitors. *J. Alloys Compd.* 742, 844–851.
- Ilyas, A.M., Gondal, M.A., Baig, U., Akhtar, S., Yamani, Z.H., 2016. Photovoltaic performance and photocatalytic activity of facile synthesized graphene decorated TiO<sub>2</sub> monohybrid using nanosecond pulsed ablation in liquid technique. *Sol. Energy* 137, 246–255.
- Jin, J., Yu, J., Guo, D., Cui, C., Ho, W., 2015. A Hierarchical Z-Scheme CdS-WO<sub>3</sub> Photocatalyst with Enhanced CO<sub>2</sub> Reduction Activity. *Small* 11, 5262–5271.
- Jing, C., Guo, X., Xia, L., Chen, Y., Wang, X., Liu, X., Dong, B., Dong, F., Li, S., Zhang, Y., 2020a. Morphologically confined hybridization of tiny CoNi<sub>2</sub>S<sub>4</sub> nanosheets into S, P co-doped graphene leading to enhanced pseudocapacitance and rate capability. *Chem. Eng. J.* 379, 122305.
- Jing, C., Liu, X.D., Li, K., Liu, X., Dong, B., Dong, F., Zhang, Y., 2020b. The Pseudocapacitance Mechanism of Graphene/CoAl LDH and Its Derivatives: are All the Modifications Beneficial? *J. Energy Chem.* 52, 218–227. <https://doi.org/10.1016/j.jchem.2020.04.019>.
- Jing, C., Song, X., Li, K., Zhang, Y., Liu, X., Dong, B., Dong, F., Zhao, S., Yao, H., Zhang, Y., 2020c. Optimizing the rate capability of nickel cobalt phosphide nanowires on graphene oxide by the outer/inter-component synergistic effects. *J. Mater. Chem. A* 8 (4), 1697–1708. <https://doi.org/10.1039/C9TA12192G>.
- Kang, Y., Chu, Z., Zhang, D., Li, G., Jiang, Z., Cheng, H., Li, X., 2013. Incorporate boron and nitrogen into graphene to make BCN hybrid nanosheets with enhanced microwave absorbing properties. *Carbon N. Y.* 61, 200–208.
- Levendorf, M.P., Kim, C.-J., Brown, L., Huang, P.Y., Havener, R.W., Muller, D.A., Park, J., 2012. Graphene and boron nitride lateral heterostructures for atomically thin circuitry. *Nature* 488, 627.
- Li, T., Jiao, X., You, T., Dai, F., Zhang, P., Yu, F., Hu, L., Ding, L., Zhang, L., Wen, Z., 2019. Hexagonal boron nitride nanosheet/carbon nanocomposite as a high-performance cathode material towards aqueous asymmetric supercapacitors. *Ceram. Int.* 45, 4283–4289.
- Li, W., Liu, J., Zhao, D., 2016a. Mesoporous materials for energy conversion and storage devices. *Nat. Rev. Mater.* 1, 16023.
- Li, Y., Wang, G., Wei, T., Fan, Z., Yan, P., 2016b. Nitrogen and sulfur co-doped porous carbon nanosheets derived from willow catkin for supercapacitors. *Nano Energy* 19, 165–175.
- Liu, B., Yan, S., Song, Z., Liu, M., Ji, X., Yang, W., Liu, J., 2016. One-step synthesis of boron nitride quantum dots: Simple chemistry meets delicate nanotechnology. *Chem. Eur. J.* 22, 18899–18907.
- Liu, P., Sui, Y., Wei, F., Qi, J., Meng, Q., Ren, Y., He, Y., 2019. Facile synthesis of CoNi<sub>2</sub>S<sub>4</sub> nanoparticles grown on carbon fiber cloth for supercapacitor application. *J. Mater. Sci. Mater. Electron.*, 1–10.
- Liu, Y., Zhang, M., Wang, L., Hou, Y., Guo, C., Xin, H., Xu, S., 2020. A biomass carbon material with microtubule bundling and natural O-doping derived from goldenberry calyx and its electrochemical performance in supercapacitor. *Chinese Chem. Lett.* 31, 805–808.
- Lu, Q., Xu, Y.Y., Mu, S.J., Li, W.C., 2017. The effect of nitrogen and/or boron doping on the electrochemical performance of non-caking coal-derived activated carbons for use as supercapacitor electrodes. *Xinxing Tan Cailiao/New Carbon Mater.* 32, 442–450. [https://doi.org/10.1016/S1872-5805\(17\)60133-1](https://doi.org/10.1016/S1872-5805(17)60133-1).
- Lv, B., Li, P., Liu, Y., Lin, S., Gao, B., Lin, B., 2018. Nitrogen and phosphorus co-doped carbon hollow spheres derived from polypyrrole for high-performance supercapacitor electrodes. *Appl. Surf. Sci.* 437, 169–175.
- Ma, X., Ning, G., Sun, Y., Pu, Y., Gao, J., 2014. High capacity Li storage in sulfur and nitrogen dual-doped graphene networks. *Carbon N. Y.* 79, 310–320.
- Maity, C.K., Hatui, G., Sahoo, S., Saren, P., Nayak, G.C., 2019. Boron Nitride based Ternary Nanocomposites with Different Carbonaceous Materials Decorated by Polyaniline for Supercapacitor Application. *ChemistrySelect* 4, 3672–3680.

- Moqbel, R.A., Gondal, M.A., Qahtan, T.F., Dastageer, M.A., 2018a. Pulsed laser synthesis in liquid of efficient visible-light-active ZnO/rGO nanocomposites for improved photo-catalytic activity. *Mater. Res. Express* 5, 35050.
- Moqbel, R.A., Gondal, M.A., Qahtan, T.F., Dastageer, M.A., 2018b. Synthesis of cadmium sulfide-reduced graphene oxide nanocomposites by pulsed laser ablation in liquid for the enhanced photocatalytic reactions in the visible light. *Int. J. Energy Res.* 42, 1487–1495.
- Nasini, U.B., Bairi, V.G., Ramasahayam, S.K., Bourdo, S.E., Viswanathan, T., Shaikh, A.U., 2014. Phosphorous and nitrogen dual heteroatom doped mesoporous carbon synthesized via microwave method for supercapacitor application. *J. Power Sources* 250, 257–265.
- Panchakarla, L.S., Govindaraj, A., Rao, C.N.R., 2007. Nitrogen-and boron-doped double-walled carbon nanotubes. *ACS Nano* 1, 494–500.
- Papagiannouli, I., Aloukos, P., Rioux, D., Meunier, M., Couris, S., 2015. Effect of the Composition on the Nonlinear Optical Response of  $Au_x Ag_{1-x}$  Nano-Alloys. *J. Phys. Chem. C* 119, 6861–6872.
- Pell, W.G., Conway, B.E., 2001. Voltammetry at a de Levie brush electrode as a model for electrochemical supercapacitor behaviour. *J. Electroanal. Chem.* 500, 121–133.
- Peng, Z., Hu, Y., Wang, J., Liu, S., Li, C., Jiang, Q., Lu, J., Zeng, X., Peng, P., Li, F., 2019. Fullerene-Based In Situ Doping of N and Fe into a 3D Cross-Like Hierarchical Carbon Composite for High-Performance Supercapacitors. *Adv. Energy Mater.* 9, 1802928.
- Pham, H.T.T., Kim, Y., Kim, Y.-J., Lee, J., Park, M., 2019. Robust Design of Dual-Phasic Carbon Cathode for Lithium-Oxygen Batteries. *Adv. Funct. Mater.* 29, 1902915.
- Saha, S., Jana, M., Khanra, P., Samanta, P., Koo, H., Murmu, N.C., Kuila, T., 2015. Band gap engineering of boron nitride by graphene and its application as positive electrode material in asymmetric supercapacitor device. *ACS Appl. Mater. Interfaces* 7, 14211–14222. <https://doi.org/10.1021/acsami.5b03562>.
- Shih, C.-Y., Wu, C., Shugaev, M.V., Zhigilei, L.V., 2017. Atomistic modeling of nanoparticle generation in short pulse laser ablation of thin metal films in water. *J. Colloid Interface Sci.* 489, 3–17.
- Sonmez, G., Schottland, P., Reynolds, J.R., 2005. PEDOT/PAMPS: An electrically conductive polymer composite with electrochromic and cation exchange properties. *Synth. Met.* 155, 130–137.
- Walter, J.G., Petersen, S., Stahl, F., Scheper, T., Barcikowski, S., 2010. Laser ablation-based one-step generation and bio-functionalization of gold nanoparticles conjugated with aptamers. *J. Nanobiotechnology* 8, 21.
- Wang, X., Zhang, Y., Zheng, J., Jiang, H., Dong, X., Liu, X., Meng, C., 2020. Fabrication of vanadium sulfide ( $VS_4$ ) wrapped with carbonaceous materials as an enhanced electrode for symmetric supercapacitors. *J. Colloid Interface Sci.*
- Wu, C.-C., Huang, S.-T., Tseng, T.-W., Rao, Q.-L., Lin, H.-C., 2010a. FT-IR and XRD investigations on sintered fluorinated hydroxyapatite composites. *J. Mol. Struct.* 979, 72–76.
- Wu, S., Zhu, Y., 2017. Highly densified carbon electrode materials towards practical supercapacitor devices. *Sci. China Mater.* 60, 25–38.
- Wu, X., Zhai, Z.-B., Huang, K.-J., Ren, R.-R., Wang, F., 2020a. Boosting energy and power performance of aqueous energy storage by engineering ultra-fine metallic  $VSe_2$  nanoparticles anchored reduced graphene oxide. *J. Power Sources* 448, 227399.
- Wu, Y., Liu, X., Xia, D., Sun, Q., Yu, D., Sun, S., Liu, X., Teng, Y., Zhang, W., Zhao, X., 2020b. Synthesis of few-layer N-doped graphene from expandable graphite with melamine and its application in supercapacitors. *Chinese Chem. Lett.* 31, 559–564.
- Wu, Y.P., Fang, S., Jiang, Y., Holze, R., 2002. Effects of doped sulfur on electrochemical performance of carbon anode. *J. Power Sources* 108, 245–249.
- Wu, Z., Wang, D., Ren, W., Zhao, J., Zhou, G., Li, F., Cheng, H., 2010b. Anchoring hydrous  $RuO_2$  on graphene sheets for high-performance electrochemical capacitors. *Adv. Funct. Mater.* 20, 3595–3602.
- Xiao, X., Zou, L., Pang, H., Xu, Q., 2020. Synthesis of micro/nanoscaled metal-organic frameworks and their direct electrochemical applications. *Chem. Soc. Rev.* 49, 301–331.
- Xie, B., Wang, Y., Lai, W., Lin, W., Lin, Z., Zhang, Z., Zou, P., Xu, Y., Zhou, S., Yang, C., 2016. Laser-processed graphene based micro-supercapacitors for ultrathin, rollable, compact and designable energy storage components. *Nano Energy* 26, 276–285.
- Xing, L.-L., Huang, K.-J., Cao, S.-X., Pang, H., 2018a. Chestnut shell-like  $Li_4Ti_5O_{12}$  hollow spheres for high-performance aqueous asymmetric supercapacitors. *Chem. Eng. J.* 332, 253–259.
- Xing, L.-L., Wu, X., Huang, K.-J., 2018b. High-performance supercapacitor based on three-dimensional flower-shaped  $Li_4Ti_5O_{12}$ -graphene hybrid and pine needles derived honeycomb carbon. *J. Colloid Interface Sci.* 529, 171–179.
- Xu, L., Jia, M., Li, Y., Zhang, S., Jin, X., 2017. Design and synthesis of graphene/activated carbon/polypyrrole flexible supercapacitor electrodes. *Rsc Adv.* 7, 31342–31351.
- Xue, Y., Liu, Q., He, G., Xu, K., Jiang, L., Hu, X., Hu, J., 2013. Excellent electrical conductivity of the exfoliated and fluorinated hexagonal boron nitride nanosheets. *Nanoscale Res. Lett.* 8, 49.
- Yadav, N., Yadav, N., Hashmi, S.A., 2020. Ionic liquid incorporated, redox-active blend polymer electrolyte for high energy density quasi-solid-state carbon supercapacitor. *J. Power Sources* 451, 227771.
- Yan, J., Wei, T., Shao, B., Ma, F., Fan, Z., Zhang, M., Zheng, C., Shang, Y., Qian, W., Wei, F., 2010. Electrochemical properties of graphene nanosheet/carbon black composites as electrodes for supercapacitors. *Carbon N. Y.* 48, 1731–1737.
- Yang, N., Xu, C., Hou, J., Yao, Y., Zhang, Q., Grami, M.E., He, L., Wang, N., Qu, X., 2016. Preparation and properties of thermally conductive polyimide/boron nitride composites. *RSC Adv.* 6, 18279–18287.
- Yang, Z., Dai, Y., Wang, S., Cheng, H., Yu, J., 2015. In situ incorporation of a S, N doped carbon/sulfur composite for lithium sulfur batteries. *RSC Adv.* 5, 78017–78025.
- Yu, M., Shao, H., Wang, G., Yang, F., Liang, C., Rozier, P., Wang, C.-Z., Lu, X., Simon, P., Feng, X., 2020. Interlayer gap widened  $\alpha$ -phase molybdenum trioxide as high-rate anodes for dual-ion-intercalation energy storage devices. *Nat. Commun.* 11, 1–9.
- Yun, S.-M., Kim, J.-W., Jung, M.-J., Nho, Y.-C., Kang, P.-H., Lee, Y.-S., 2007. An XPS Study of Oxyfluorinated Multiwalled Carbon Nano Tubes. *Carbon Lett.* 8, 292–298. <https://doi.org/10.5714/cl.2007.8.4.292>.
- Zeng, H., Du, X., Singh, S.C., Kulinich, S.A., 2012. Nanomaterials via Laser Ablation / Irradiation in Liquid. A Review 1333–1353. <https://doi.org/10.1002/adfm.201102295>.
- Zeng, H., Duan, G., Li, Y., Yang, S., Xu, X., Cai, W., 2010. Blue Luminescence of ZnO nanoparticles based on non-equilibrium processes: defect origins and emission controls. *Adv. Funct. Mater.* 20, 561–572.
- Zhai, Z.-B., Huang, K.-J., Wu, X., Hu, H., Xu, Y., Chai, R.-M., 2019. Metal-organic framework derived small sized metal sulfide nanoparticles anchored on N-doped carbon plates for high-capacity energy storage. *Dalt. Trans.* 48, 4712–4718.
- Zhang, X., Sui, Y., Wei, F., Qi, J., Meng, Q., Ren, Y., He, Y., 2019a. Self-supported 3D layered zinc/nickel metal-organic-framework with enhanced performance for supercapacitors. *J. Mater. Sci. Mater. Electron.* 30, 18101–18110.
- Zhang, Y., Liu, J., Li, S.-L., Su, Z.-M., Lan, Y.-Q., 2019b. Polyoxometalate-based materials for sustainable and clean energy conversion and storage. *EnergyChem* 100021.
- Zhao, X., Cai, W., Yang, Y., Song, X., Neale, Z., Wang, H.-E., Sui, J., Cao, G., 2018.  $MoSe_2$  nanosheets perpendicularly grown on

- graphene with Mo–C bonding for sodium-ion capacitors. *Nano Energy* 47, 224–234.
- Zheng, J., Zhang, Y., Wang, Q., Jiang, H., Liu, Y., Lv, T., Meng, C., 2018. Hydrothermal encapsulation of VO<sub>2</sub> (A) nanorods in amorphous carbon by carbonization of glucose for energy storage devices. *Dalt. Trans.* 47, 452–464.
- Zheng, S., Li, Q., Xue, H., Pang, H., Xu, Q., 2020. A highly alkaline-stable metal oxide@ metal–organic framework composite for high-performance electrochemical energy storage. *Natl. Sci. Rev.* 7, 305–314.
- Zheng, X., Wang, G., Huang, F., Liu, H., Gong, C., Wen, S., Hu, Y., Zheng, G., Chen, D., 2019. Liquid Phase Exfoliated Hexagonal Boron Nitride/Graphene Heterostructure Based Electrode Toward Asymmetric Supercapacitor Application. *Front, Chem*, p. 7.